History-Augmented Contrastive Meta-Learning for Unsupervised Blind Super-Resolution of Planetary Remote Sensing Images

Huijia Zhao O, Student Member, IEEE, Jie Lu, Yunqing Jiang, Xiao-Ping Lu* O, Kaichang Di

Abstract-Planetary remote sensing images are affected by diverse and unknown degradations caused by imaging environments and hardware constraints. These factors limit image quality and hinder supervised blind super-resolution due to the lack of ground-truth images. This work presents History-Augmented Contrastive Blind Super-Resolution (HACBSR), an unsupervised framework for blind super-resolution that operates without ground-truth images and external kernel priors. HACBSR comprises two components: (1) a contrastive kernel sampling mechanism with kernel similarity control to mitigate distribution bias from Gaussian sampling, and (2) a historyaugmented contrastive learning that uses historical models to generate negative samples to enable less greedy optimization and to induce strong convexity without ground-truth. A convergence analysis of the history-augmented contrastive learning is given in the Appendix. To support evaluation in planetary applications, we introduce Ceres-50, a dataset with diverse geological features simulated degradation patterns. Experiments show that HACBSR achieves competitive performance compared with state-of-the-art unsupervised methods across multiple upscaling factors. The code is available at https://github.com/2333repeat/HACBSR, and the dataset is available at https://github.com/2333repeat/Ceres-50.

Index Terms—Meta-learning, contrastive learning, blind super-resolution, planetary remote sensing

I. INTRODUCTION

LANETARY remote sensing images serve as a foundation for understanding the geological and morphological characteristics of celestial bodies beyond Earth. These images enable scientists to conduct comparative planetary studies, analyze surface features, and investigate the geological evolution of planets and moons throughout the solar system. However, acquiring high-quality planetary images presents

This work was supported in part by the Science and Technology Development Fund, Macau SAR under Grants 0096/2022/A and 0026/2025/RIA1, and in part by the National Key Research and Development Program of China under Grant 2022YFF0503100. (Corresponding author: Xiaoping Lu.)

Huijia Zhao is with the School of Computer Science and Engineering, Macau University of Science and Technology, Taipa, Macao, China (e-mail:3240001399@student.must.edu.mo).

Jie Lu is with the School of Computer Science and Engineering, Macau University of Science and Technology, Taipa, Macao, China (e-mail:jiel13@student.must.edu.mo).

Yunqing Jiang is with the School of Computer Science and Engineering, Macau University of Science and Technology, Taipa, Macao, China (e-mail:3240007841@student.must.edu.mo).

Xiao-Ping Lu is with the School of Computer Science and Engineering, Macau University of Science and Technology, Taipa, Macao, China, and also with the State Key Laboratory of Lunar and Planetary Sciences, Macau University of Science and Technology, Taipa, Macao, China (e-mail: xplu@must.edu.mo).

Kaichang Di is with the State Key Laboratory of Remote Sensing Science, Aerospace Information Research Institute, Chinese Academy of Sciences, Beijing 100101 China (e-mail: dikc@aircas.ac.cn).

technical challenges that differ from terrestrial remote sensing. Deep space missions operate under severe constraints that directly impact imaging capabilities. Spacecraft payload limitations restrict the size and complexity of imaging systems, while extreme distances introduce significant communication delays and bandwidth restrictions. Power constraints further limit the operational capacity of imaging sensors, forcing trade-offs between spatial resolution, temporal coverage, and data transmission rates. These engineering realities result in planetary images that often exhibit insufficient resolution for detailed scientific analysis. The imaging environments across different planetary bodies present unique degradation patterns that compound these technical limitations. Martian observations contend with frequent dust storms that introduce atmospheric scattering and obscure surface features. Venus presents an even more challenging scenario, where dense sulfuric acid clouds and extreme surface temperatures create complex optical distortions. The icy moons of Jupiter and Saturn introduce additional complications through ice crystal scattering, plasma interference from radiation belts, and tidal deformation effects. Each planetary environment requires adaptive image enhancement strategies that can accommodate diverse and often unknown degradation processes.

To address these requirements, super-resolution (SR) has emerged as a viable solution. However, early SR methods primarily focused on bicubic degradation [1]–[5]. Our prior work also investigated neural operators in planetary remote sensing SR under bicubic downsampling [6]. However, degradation in real planetary remote sensing images is unknown and complex. Furthermore, blind super-resolution (BSR) represents a more realistic framework for planetary image enhancement, as it addresses scenarios where the degradation process is unknown or partially observable. A typical degradation process of BSR can be described as follows:

$$\mathbf{y} = (\mathbf{x} \otimes \mathbf{k}) \downarrow_s + \mathbf{z},\tag{1}$$

where $\mathbf{y} \in \mathbb{R}^{H \times W}$ is the observed low-resolution (LR) image, $\mathbf{x} \in \mathbb{R}^{sH \times sW}$ is the unknown high-resolution (HR) image, \otimes denotes 2D convolution, \downarrow_s denotes downsampling by factor s, $\mathbf{k} \in \mathbb{R}^{K \times K}$ is an unknown blur kernel, and \mathbf{z} denotes the additive noise. Beyond the degradation, current BSR methods can be broadly grouped into two paradigms: joint optimization approaches that simultaneously estimate degradation kernels and reconstruct high-resolution images [2], [7]–[10], and alternating optimization frameworks that decouple kernel estimation from image reconstruction [11]–[14]. While these methods report strong results on natural

images, their application to planetary remote sensing remains limited.

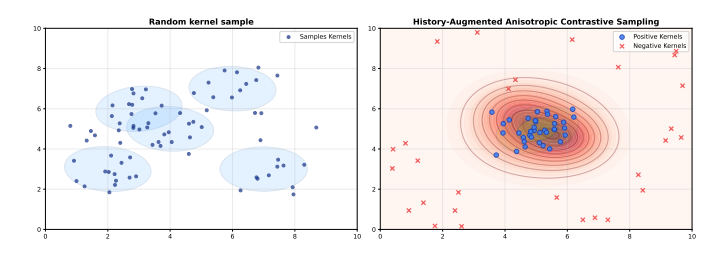


Fig. 1. Comparison of kernel distribution between random kernel samples and contrastive kernel sampling. The contrastive kernel sampling effectively generates kernels with balanced distribution. It also reduces the probability of generating outlier kernels, which can adversely affect image reconstruction.

First, existing BSR methods rely heavily on supervised training. Most deep learning-based BSR methods are constrained by their dependence on ground-truth images or kernel priors [8], [15]–[18]. However, in planetary remote sensing, acquiring large datasets is challenging and ground truth images are impossible to obtain. Therefore, developing a method that does not rely on supervised training is essential. Second, Planetary remote sensing images exhibit diverse and often unknown degradations due to dramatically different imaging environments across celestial bodies. Mars observations are compromised by dust storms that create atmospheric scattering and infrared thermal radiation artifacts, while Venus imaging must contend with dense cloud cover occlusion, sulfuric acid haze, and extreme high-temperature effects. Jupiter's moons present different degradation patterns including ice crystal scattering, plasma interference, and tidal deformation distortions. Different planetary remote sensing images exhibit different degradation patterns. Therefore, it is necessary to develop a BSR method that does not rely on presupposed kernel priors. Third, the planetary remote sensing domain lacks BSR datasets. The lack of planetary remote sensing datasets significantly hinders development in this area. The evaluation of planetary remote sensing image restoration tasks also requires BSR datasets.

Although existing BSR methods have achieved strong performance, early research has focused primarily on reconstructing HR images and estimating image degradation with a single model [8], [16]-[19]. Separating the image degradation estimation and HR image reconstruction processes has emerged as an alternative approach and has also achieved strong performance [7], [12], [20]. However, most BSR methods are trained and evaluated on datasets sharing the same degradation kernel distribution, often assuming that training and test kernels are matched or relying on kernel priors [2], [16], [21]. When these methods encounter training and test datasets with different degradation models, their performance degrades. Therefore, an unsupervised BSR method is needed that can reconstruct images without presupposed degradation kernels and handle images with different degradation kernels. Existing unsupervised BSR methods generate kernels primarily by sampling key parameters from uniform distributions [11], [13], [14], which may lead to unbalanced kernel distributions, as shown in Figure 1, potentially resulting in outlier kernels that are detrimental to reconstruction. Furthermore, since ground truth images do not participate in training and inference, the lack of supervised information may cause overly aggressive optimization, potentially leading to overfitting.

To overcome these limitations, we propose History-Augmented Contrastive Blind Super-Resolution (HACBSR), an unsupervised BSR model that does not rely on groundtruth images or degradation kernel priors. HACBSR incorporates contrastive kernel sampling in the kernel learning (KL) stage and history-augmented contrastive learning with meta-learning in the contrastive image learning (CIL) stage. Unlike previous alternating optimization unsupervised BSR approaches, the contrastive kernel sampling overcomes the kernel bias generated from random explicit Gaussian sampling, as shown in Fig. 1, and balances the kernel distribution to provide improved kernel priors and achieve more general parameters for the next stage of optimization. The historyaugmented contrastive learning provides self-prior guidance from the historical image estimator to supply additional contrastive supervision. Introducing historical information enables a less aggressive optimization strategy and a more compact optimization space. In contrast to prior BSR work, HACBSR learns a kernel generator and regulates it using contrastive kernel sampling to reduce outlier kernels during alternating optimization. Furthermore, HACBSR applies historical contrast jointly to the image and kernel pathways, coupled with observation consistency, which is critical without paired supervision.

The main contributions of this article can be described as follows:

- We propose History-Augmented Contrastive Blind Super-Resolution (HACBSR), the first unsupervised planetary remote sensing BSR method, which performs blind super-resolution without ground-truth images or kernel priors.
- 2) We propose contrastive kernel sampling to balance diversity and plausibility, reducing outlier kernels, and a history-augmented contrastive learning that regularizes image pathways under observation consistency, stabilizing training without paired supervision. Furthermore, we provide stability analysis to prove that the history-augmented contrastive learning improves convergence in feature space.
- 3) We propose the Ceres-50 dataset, the first open-source planetary remote sensing BSR dataset. It includes 50 Ceres images degraded by random Gaussian kernels with random noise and additive Gaussian noise. On Ceres-50, HACBSR achieves competitive performance across scales against state-of-the-art unsupervised BSR methods.

II. RELATED WORK

A. Non-blind Super-resolution

Non-blind super-resolution focuses on reconstructing images under bicubic degradation [22], [23]. SRCNN was the first deep learning-based end-to-end super-resolution method [1]. Residual connections have enabled deep neural networks

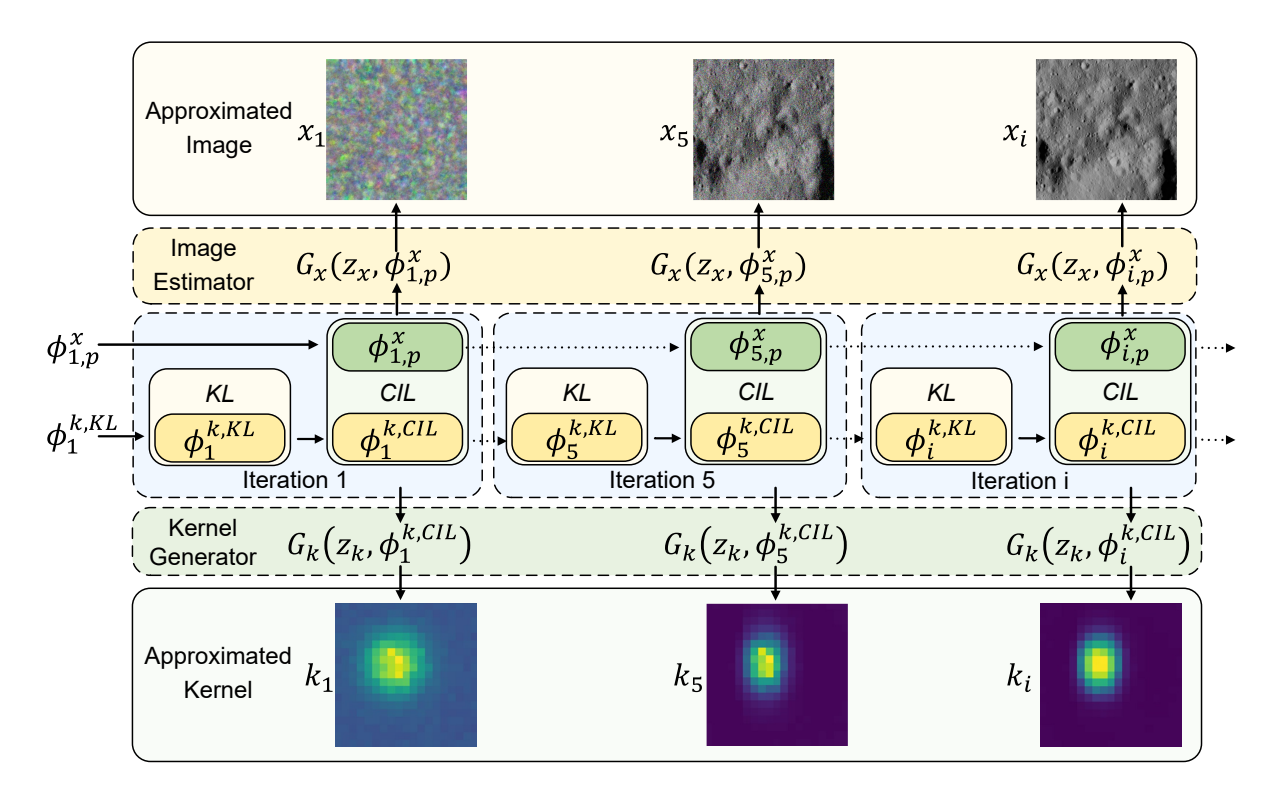


Fig. 2. Overall workflow of the proposed framework. The Kernel learning (KL) stage and Contrastive Image Learning (CIL) stage will be optimized alternately. In KL stage, the parameter of kernel generator $\phi_i^{k,CIL}$ will be optimized. In CIL stage, the parameter of kernel generator and image estimator $\phi_i^{k,CIL}$ and $\phi_{i,1}^x$ will be optimized. After the N-th iteration, the image estimator and the kernel generator generate the SR image x_N and the output kernel k_N as the final output. The detailed algorithm is presented in Algorithm 1.

in the super-resolution domain [3], [16], [24]–[26]. In remote sensing, end-to-end supervised learning and specialized neural network designs have become popular [27], [28]. Additionally, ZSSR achieves unsupervised super-resolution through deep internal learning [29], while meta-learning improves convergence by finding initialization-sensitive weights [30].

B. Blind Super-resolution

Unlike non-blind SR, BSR reconstructs images under degradation kernels and additive noise instead of bicubic downsampling, achieving more complex and realistic degradation [15], [31], [32]. In BSR, kernel estimation plays an important role prior to image reconstruction, with image reconstruction typically conducted after kernel estimation [15], [33]. KernelGAN estimates the degradation kernel through image internal recurrence [7]. Decoupling features through contrastive learning to focus on resolution-invariant features while ignoring resolution-variant features also yields strong performance [34]. Pre-trained BSR models have achieved strong performance in remote sensing applications [9], [10], [35]-[37]. For unsupervised BSR, Flow-based Kernel Prior (FKP) leverages normalizing flows to learn the mapping between Gaussian kernel distributions and latent variables [11]. Combining meta-learning with random kernel generators also achieves strong performance [14]. Simulating degradation kernels with Markov Chain Monte Carlo and using Langevin dynamics to optimize the network also mitigate the overfitting [13].

C. Contrastive Learning

Beyond supervised learning and self-supervised learning, the contrastive learning has achieved strong performance across various tasks [38]. Contrastive learning focuses on learning common features between similar objects and distinguishing features from dissimilar objects [38], [39]. Classifying images based on non-parametric instance similarity achieves strong performance [40]. By constructing a dynamic queue, Momentum Contrast (MoCo) achieves strong performance in unsupervised visual representation learning [41]. In BSR, generating negative samples from a neural network with historical parameters provides a model-level contrastive learning solution [42]. Extracting resolution-invariant information through contrastive decoupling encoding and achieving feature refinement with contrastive learning also yields strong image reconstruction performance [34].

III. METHOD

A. Model overview

The overall framework of HACBSR is shown in Figure 2, and the detailed procedure is provided in Algorithm 1. HACBSR comprises two network structures: a kernel generator $G_k(\cdot)$ with parameters ϕ^k and an image estimator $G_x(\cdot)$ with parameters ϕ^x . For clarity, stage-specific parameters of the kernel generator are annotated with the stage name. At the i-th iteration, in the KL stage, the kernel generator parameters are denoted by $\phi_i^{k,\mathrm{KL}}$; in the CIL stage, the kernel

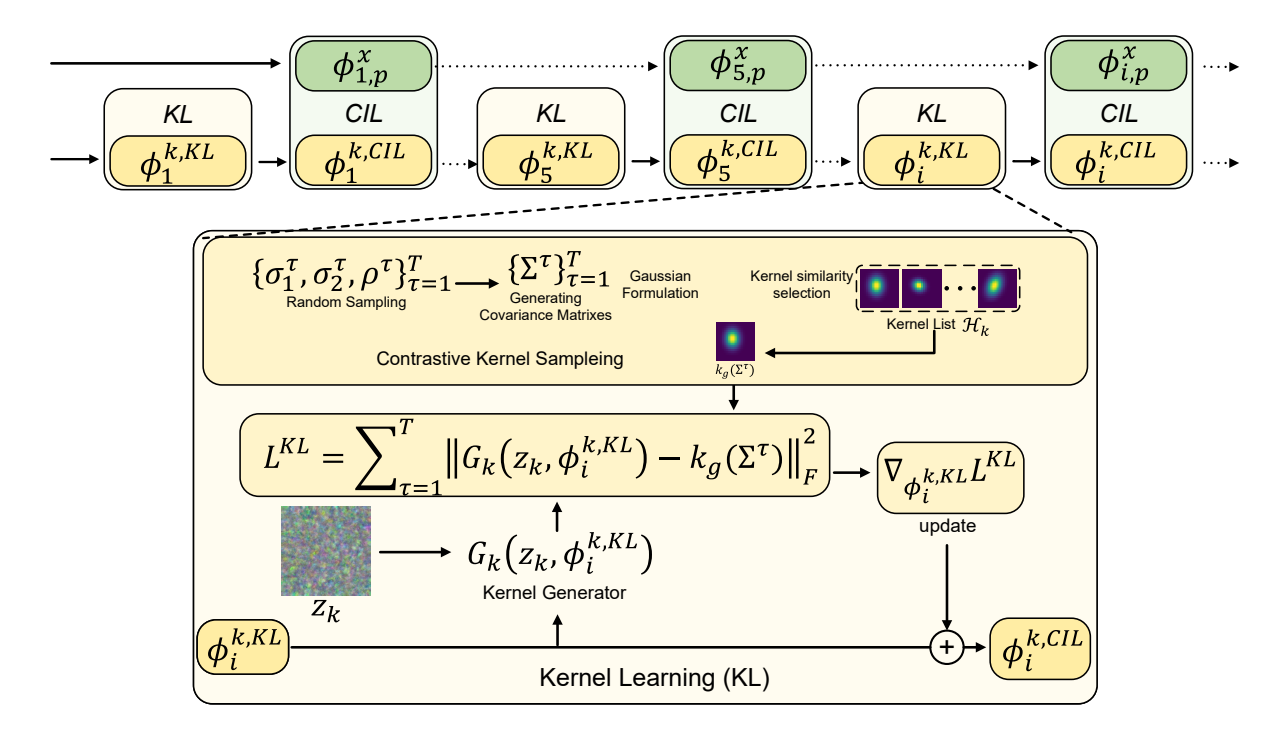


Fig. 3. Overall workflow of the KL stage. In the KL stage, the Contrastive Kernel sampling the degradation kernel with similarity control, and then the kernel generator $G_k(\cdot)$ is optimized with these kernels to provide a kernel prior. The z_k denotes the random noise.

generator parameters are denoted by $\phi_i^{k,\mathrm{CIL}}$, and the image estimator parameters are denoted by $\phi_{i,1}^x$. HACBSR is built on alternating optimization between the Kernel Learning (KL) stage over $\phi_i^{k,\mathrm{KL}}$ and the Contrastive Image Learning (CIL) stage over $\phi_i^{k,\mathrm{CIL}}$ and $\phi_{i,1}^x$. The detail of KL stage is shown in section III-B and the detail of CIL stage is shown in section III-C. After N-th iteration optimization, the $G_k(\cdot)$ will generate estimated kernel k_N and $G_x(\cdot)$ will generate SR image x_N .

B. Kernel Learning

The contrastive kernel sampling addresses a fundamental limitation of random Gaussian parameter sampling illustrated in Figure 1: purely random selection from uniform distributions often produces unbalanced kernel distributions with outliers that destabilize subsequent image reconstruction. To ensure the kernel list \mathcal{H}_k contains diverse yet plausible samples, we propose a similarity-guided rejection sampling mechanism which named Contrastive Kernel Sampling that evaluates each candidate kernel against the recent kernel history.

In the Kernel Learning stage, the kernel generator $G_k(\cdot)$ is optimized using kernels from contrastive kernel sampling to provide a degradation kernel prior for image reconstruction and to control the relaxation of the kernel generator. The detailed algorithm for KL is shown in Algorithm 1 and Figure 3. In this stage, given a batch of candidate kernels $\{k_g(\Sigma_\tau)\}_{\tau=1}^T$ from the kernel list \mathcal{H}_k sampled by Contrastive Kernel Sampling as the explicit kernel prior, a shallow fully connected network (FCN) is chosen as the kernel generator. The parameters of the kernel generator at the i-th iteration in the KL stage are denoted as $\phi_i^{k,KL}$. The $G_k(\cdot)$ generates

the degradation kernel from random noise z_k and is optimized with $k_q(\Sigma_{\tau})$. The process follows the loss function:

$$L^{KL} = \sum_{\tau=1}^{T} \left\| G_k(z_k, \phi_i^{k, KL}) - k_g(\Sigma^{\tau}) \right\|_F^2, \tag{2}$$

where $\|\cdot\|_F$ denotes the Frobenius norm. Then the parameters of the kernel generator will be optimized and be further optimized in CIL stage:

$$\phi_i^{k,CIL} \leftarrow \phi_i^{k,KL} - \gamma_k^{KL} \cdot \text{Adam}\left(\frac{\partial L^{KL}}{\partial \phi_i^{k,KL}}\right),$$
 (3)

where the γ_k^{KL} denotes the learning rate. Minimizing $L_{\rm KL}$ enables G_k to learn a diverse yet plausible kernel prior aligned with the recent kernel list \mathcal{H}_k .

1) Contrastive Kernel Sampling: To sample the anisotropic Gaussian kernel, the coordinates $h = \begin{bmatrix} m \\ n \end{bmatrix}$ and covariance matrix $\Sigma = \begin{bmatrix} \sigma_1^2 & \rho\sigma_1\sigma_2 \\ \rho\sigma_1\sigma_2 & \sigma_2^2 \end{bmatrix}$ are sampled from a uniform distribution, where σ_1 and σ_2 represent horizontal and vertical variances, respectively. The parameter ρ denotes the correlation index, and m, n are the coordinates of the Gaussian kernel. Using the Gaussian formula, the anisotropic Gaussian kernels can be expressed as:

$$k_g(\Sigma) = \frac{1}{2\pi |\Sigma|^{\frac{1}{2}}} e^{-\frac{1}{2}(h-h_0)^T \Sigma^{-1}(h-h_0)},$$
 (4)

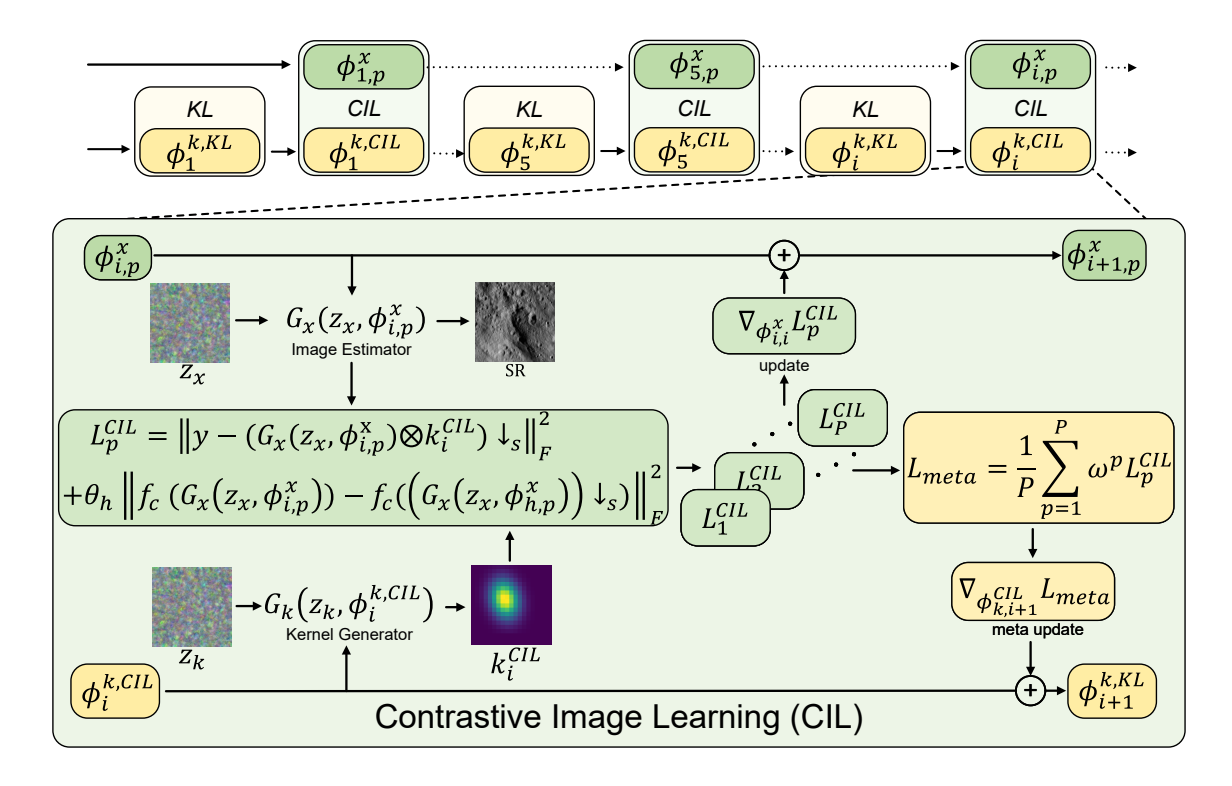


Fig. 4. Overall workflow of the Contrastive Image Learning (CIL) framework. During the CIL stage, the kernel generator and image estimator are optimized using the LR image y, where z_k and z_x denote random noise.

where h_0 denotes the coordinates of the kernel center. However, randomly sampled kernels may result in an unbalanced distribution, potentially including outlier kernels that are detrimental to kernel generator optimization and image prior estimation. To obtain candidate kernels that are diverse yet plausible, we maintain a first-in-first-out kernel list $\mathcal{H}_k = \{(\mathbf{k}_t, \mathbf{s}_t)\}_{k=1}^K$ storing recent kernels and their similarity scores. The similarity score between a candidate \mathbf{k}_c and a historical kernel \mathbf{k}_t combines Pearson correlation α_r , SSIM, and descriptor similarity $\mathbf{f}_s(\cdot, \cdot)$ based on the average of kernel statistics and spatial distribution characteristics.

$$S(\mathbf{k}_{c}, \mathbf{k}_{t}) = \alpha_{r} (\mathbf{k}_{c}, \mathbf{k}_{t}) + \alpha_{ssim} SSIM(\mathbf{k}_{c}, \mathbf{k}_{t}) + \alpha_{feat} \mathbf{f}_{s} (\mathbf{k}_{c}, \mathbf{k}_{t}),$$
(5)

where α = 0.5, $\alpha_{\rm ssim}$ =0.2 and $\alpha_{\rm feat}$ =0.3. Over a recent sliding window with 20 recent kernels, we compute $S_{\rm avg}$, $S_{\rm min}$, $S_{\rm max}$ and define a kernel similarity score as follows:

$$\mathcal{J}(\mathbf{k}_{c}) = -\left|\mathcal{S}_{avg}(\mathbf{k}_{c}) - \tau\right| - \left(\mathcal{S}_{max}(\mathbf{k}_{c}) - \sigma_{max}\right) - \left(\sigma_{min} - \mathcal{S}_{min}(\mathbf{k}_{c})\right),$$
(6)

where σ_{\min} and σ_{\max} denote the minimum and maximum similarity indices, respectively, and are set to 0.3 and 0.8. The τ denotes the target similarity index and is set to 0.3. The terms $\mathcal{S}_{\mathrm{avg}}$, $\mathcal{S}_{\mathrm{max}}$, and $\mathcal{S}_{\mathrm{min}}$ represent the average, maximum, and minimum similarity scores generated from the kernel list, respectively. This formulation encourages moderate novelty while penalizing redundancy and outliers. Among multiple random proposals, we retain the one with the largest $\mathcal{J}(\cdot)$ value and append it to \mathcal{H}_k for further training.

C. Contrastive Image Learning

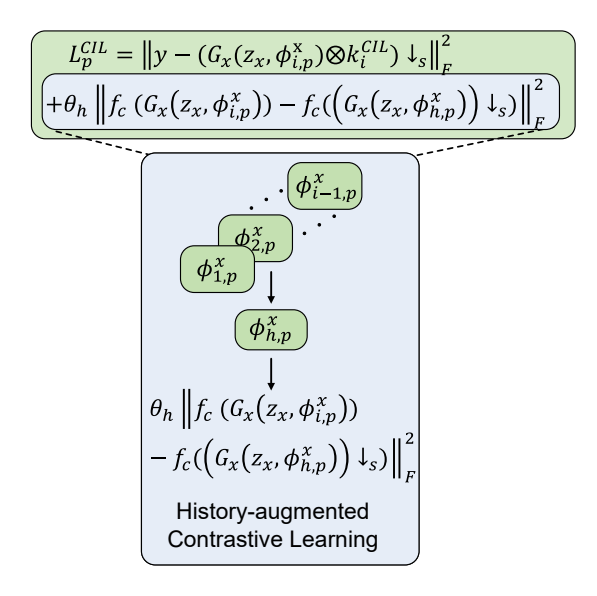


Fig. 7. Workflow of history-augmented contrastive learning. Leveraging the history model reduces greedy updates and achieves optimization toward a stronger convex.

In the CIL stage, the image estimator learns to estimate SR images while the kernel generator learns to estimate degradation kernel from the input LR image. The detail algorithm for Contrastive Image Learning is presented in Algorithm 1 and Figure 4. Under unsupervised conditions, obtaining ground truth images is impossible. Therefore, the image estimator

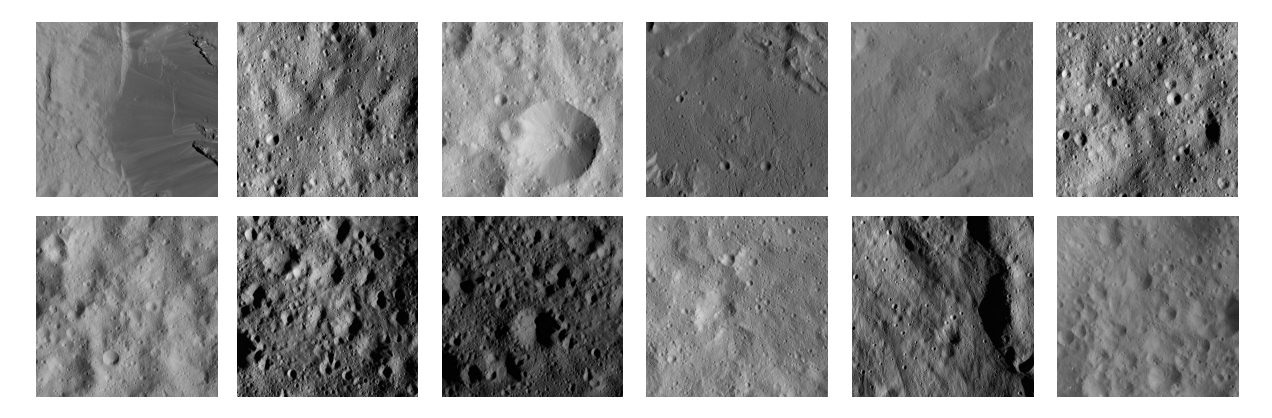


Fig. 5. Example images of the Ceres-50 dataset.

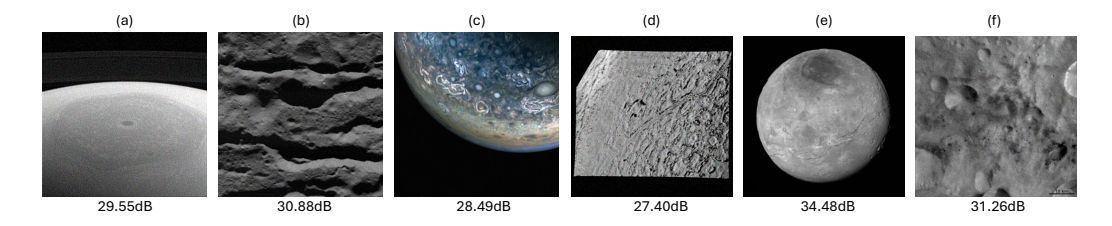


Fig. 6. Generalization test of $4 \times BSR$ results for different morphological features on various planets. (a) Saturn's northern hemisphere. (b) Deep Fractures in Occator Crater on Ceres. (c) Jupiter's surface. (d) Northern Hemisphere of Neptune. (e) Charon's Complexity. (f)Dark Material Associated with and between Craters on Vesta.

TABLE I

AVERAGE PSNR/SSIM RESULTS ON CERES-50 DATASET. AVERAGE KERNEL PSNR RESULTS ARE SHOWN IN BRACKET. BEST PERFORMANCE IS SHOWN IN BOLD.

Method	×2	×3	×4	Model Size
Bicubic	27.80/0.695	24.32/0.476	23.76/0.445	-
FKP-DIP	29.87/0.731	28.97/0.675	27.90/0.650	2359K + 143K
MLMC	32.07/0.801	30.60/0.740	29.40/0.686	2359K + 562K
HACBSR	32.21/0.816	30.96/0.763	29.87/0.720	2359K + 562K

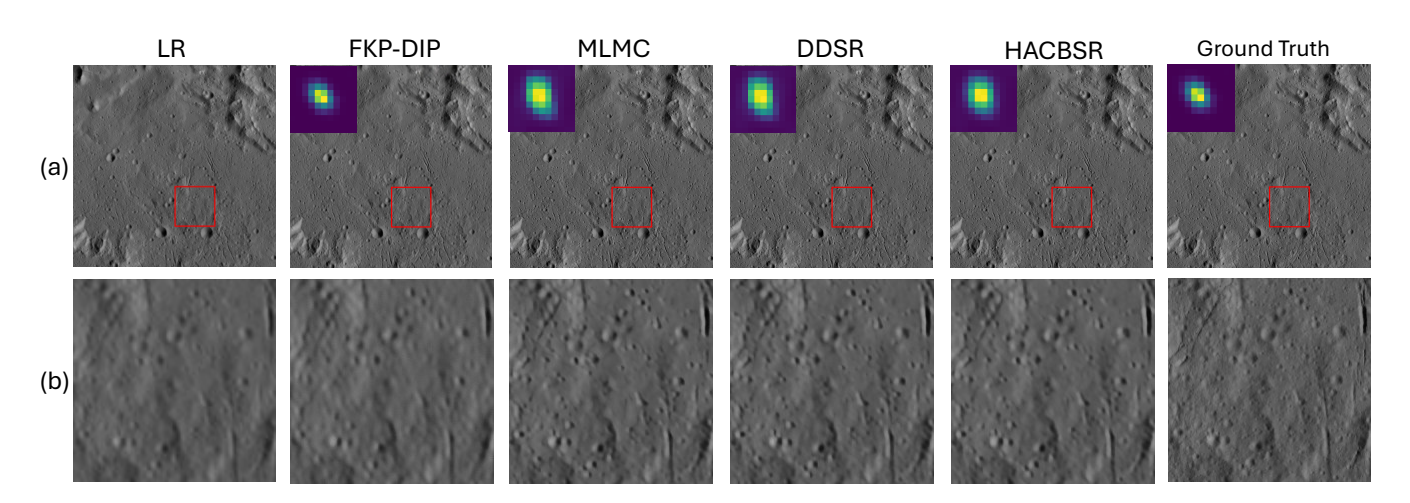


Fig. 8. Perceptual comparisons of different methods in $2\times$. The (a) include the ground truth, LR and reconstructed images, the estimated kernels are shown on top left. The (b) denote the zoomed-in for the select area from (a).

 $G_x(\cdot)$ and kernel generator $G_k(\cdot)$ are optimized using the input LR image y. In the CIL stage at the i-th iteration, the image estimator $G_x(z_x,\phi^x_{i,p})$ generates the SR image with

model parameter $\phi^x_{i,p}$ and random noise z_x . Combined with degradation kernel k_i^{CIL} generated by $G_k(z_k,\phi_i^{k,CIL})$, the

core CIL loss function is constructed as follows:

$$L_p^C = \|y - (G_x(z_x, \phi_{i,p}^x) \otimes k_i^{CIL}) \downarrow_s \|_F^2,$$
 (7)

Algorithm 1 The proposed HACBSR algorithm.

```
1: Input: Low-resolution image y.
  2: Initialize: z_k, z_x, \phi_1^{k,KL}, \phi_{1,1}^x.
  3: for i \leftarrow 1, 2, ..., N do
4: \{k_g(\Sigma^{\tau})\}_{\tau=1}^T \leftarrow \text{Contrastive Kernel Sampling}
                    L^{KL} = \sum_{\tau=1}^{T} \left\| G_k(z_k, \phi_i^{k,KL}) - k_g(\Sigma^{\tau}) \right\|_F^2
\phi_i^{k,CIL} \leftarrow \phi_i^{k,KL} - \gamma_k^{KL} \cdot \operatorname{Adam}\left(\frac{\partial L^{KL}}{\partial \phi_i^{k,KL}}\right)
k_i^{CIL} \leftarrow G_k(z_k, \phi_i^{k,CIL})
  6:
   7:
  8:
                                L_p^{CIL} = \left\| y - (G_x(z_x, \phi_{i,p}^x) \otimes k_i^{CIL}) \downarrow_s \right\|_F^2 + \theta_h \cdot
          \left\| f_c(G_x(z_x, \phi_{i,p}^x)) - f_c(G_x(z_x, \phi_{h,p}^x)) \right\|_F^2
\phi_{i,p+1}^x \leftarrow \phi_{i,p}^x - \gamma_x^{CIL} \cdot \operatorname{Adam} \left( \frac{\partial L_p^{CIL}}{\partial \phi_{i,p}^x} \right)
10:
11:
                     \begin{split} &L_{\text{Meta}} \leftarrow \tfrac{1}{P} \sum_{p=1}^{P} \omega^{p} L_{p}^{CIL} \\ &\phi_{i+1}^{k,KL} \leftarrow \phi_{i}^{k,CIL} - \gamma_{k}^{CIL} \cdot \text{Adam} \Big( \tfrac{\partial L_{\text{Meta}}}{\partial \phi_{i}^{k,CIL}} \Big) \end{split}
12:
13:
                      \phi_{i+1,1}^x \leftarrow \phi_{i,P}^x
14:
15: end for
16: Output: k_N \leftarrow G_k(z_k, \phi_{N+1}^{k,KL}), \quad x_N \leftarrow G_x(z_x, \phi_{N-P}^x)
```

where s denotes the downsample scale and y denotes the input images. To avoid overfitting, which is detrimental to unsupervised learning, history-augmented contrastive learning is introduced for the image estimator to enable less greedy optimization and construct a more compact optimization space, as shown in Figure 7. In CIL, the negative sample is generated from the image estimator with historical parameter $\phi_{h,p}^x$, while the positive sample is generated by the current image estimator $G_x(z_x, \phi_{h,p}^x)$. The negative sample provides a selfprior to achieve more robust optimization and prevents the image estimator from reconstructing overly sharpened images. Also for the kernel generator, meta-learning is introduced to reduce the random disruption of kernel sampling and guide the kernel generator parameters toward a more general position. For iteration i, let the meta-learning iteration be denoted as $p = 1, 2, 3, \dots, P$. For the p-th iteration, the CIL loss function is expressed as follows:

$$L_p^{CIL} = \|y - (G_x(z_x, \phi_{i,p}^x) \otimes k_i^{CIL}) \downarrow_s \|_F^2 + \theta_h \cdot \|f_c(G_x(z_x, \phi_{i,p}^x)) - f_c(G_x(z_x, \phi_{h,p}^x))\|_F^2,$$
(8)

where θ_h denotes the contrastive weight and is set to 0.4. The generation of $\phi_{h,p}^x$ is described in Section III-C1. The f_c denotes the encoder of CLIP [43]. The theoretical stability guarantee of this history-augmented contrastive learning is analyzed in Appendix. The parameters of the image estimator are optimized as follows:

$$\phi_{i,p+1}^x \leftarrow \phi_{i,p}^x - \gamma_x^{CIL} \cdot \text{Adam}\left(\frac{\partial L_p^{CIL}}{\partial \phi_{i,p}^x}\right),$$
 (9)

where γ_x^{CIL} denotes the learning rate of the image estimator. The main loss term $\|y-(G_x(z_x,\phi_{i,p}^x)\otimes k_i^{CIL})\downarrow_s\|_F^2$ removes the need for ground-truth supervision by computing the loss directly on the LR observation. The contrastive loss term $\theta_h \cdot \left\|f_c(G_x(z_x,\phi_{i,p}^x))-f_c(G_x(z_x,\phi_{h,p}^x))\right\|_F^2$ provides contrastive supervision for more compact optimization while incorporating historical information and prevent feature drift. The stability analysis is shown in Appendix. This approach offers a more adaptive strategy than greedy optimization. After P iterations of meta-learning, the meta loss L_{Meta} is defined:

$$L_{Meta} = \frac{1}{P} \sum_{p=1}^{P} \omega^p L_p^{CIL}.$$
 (10)

where ω^p denotes the meta-importance weight of the p-th inner-loop step. The weight ω^p is adaptively determined according to each step's core CIL loss L_p^C , which ensures that the meta-learner focuses more on informative or difficult updates instead of treating all steps equally. To stabilize the importance calculation, the loss values are first normalized as

$$\pi_p = \frac{L_p^C - \min_p L_p^C}{\sum_{p=1}^P (L_p^C - \min_p L_p^C)}.$$
 (11)

Then the meta weighting term is obtained through a logarithmic transformation:

$$\omega^{p} = -(1 - \pi_{p})^{2} \log(\pi_{p} + 10^{-3}). \tag{12}$$

The parameters of the kernel generator are then optimized as follows:

$$\phi_{i+1}^{k,KL} \leftarrow \phi_i^{k,CIL} - \gamma_k^{CIL} \cdot \text{Adam}\left(\frac{\partial L_{\text{Meta}}}{\partial \phi_i^{k,CIL}}\right),$$
 (13)

where γ_k^{CIL} denotes the meta-learning rate. The contrastive learning prevents overly greedy optimization of the image estimator while preserving historical information. meta-learning for the kernel generator enables more global and adaptive optimization instead of employing an overly greedy strategy. Through meta-learning and contrastive learning, HACBSR follows an adaptive optimization strategy that incorporates global information and leverages historical data rather than employing a greedy approach. We provide a formal stability analysis of this approach via strong convexity theory in Appendix.

1) Adaptive update of history-augmented contrastive learning: The history-augmented contrastive learning introduces a strong convexity that governs convergence stability. To achieve a balance between overfitting and convergence, the contrastive learning follow a loss-adaptive history weight update mechanism for model parameter fusion in contrastive learning. The

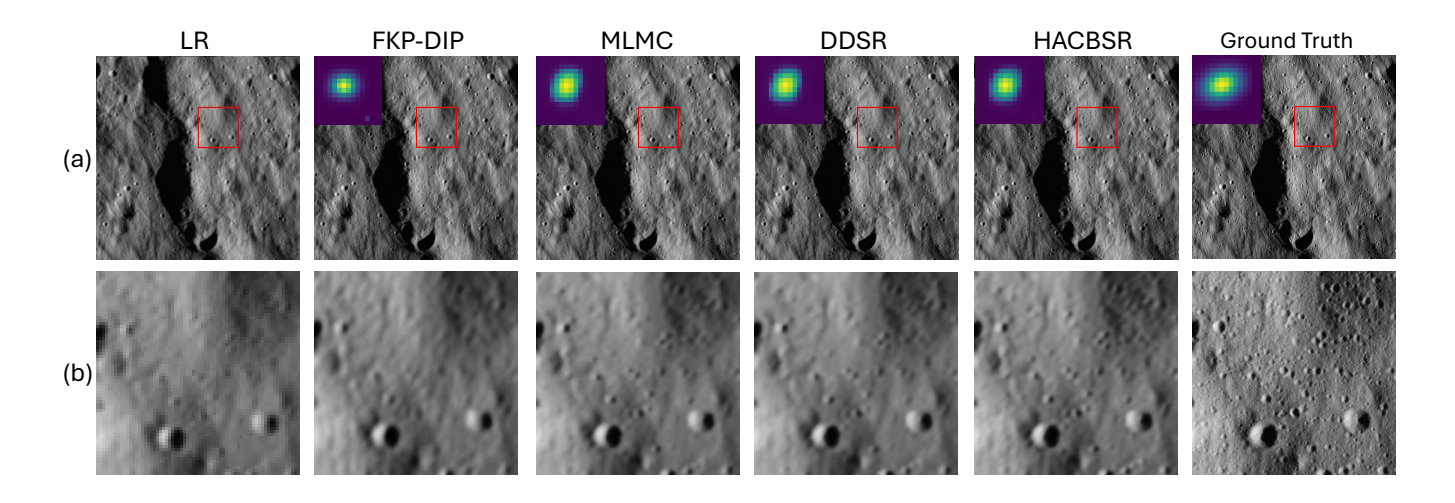


Fig. 9. Perceptual comparisons in $3\times$. The (a) include the ground truth, LR and reconstructed images, the estimated kernels are shown on top left. The (b) denote the zoomed-in for the select area from (a).

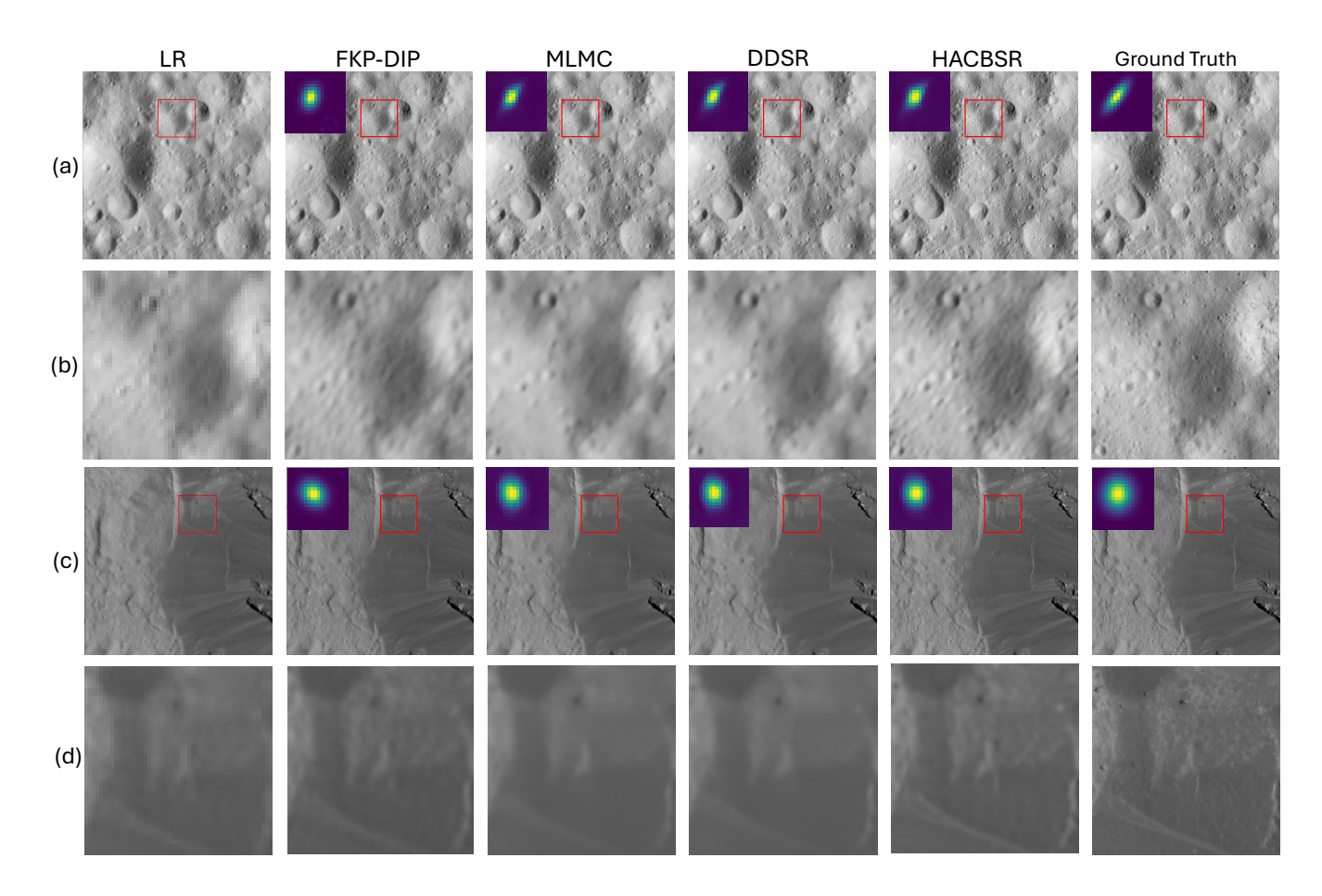


Fig. 10. Perceptual comparisons in $4\times$. The (a) (b) include the ground truth, LR and reconstructed images, the estimated kernels are shown on top left. The (c) (d) denote the zoomed-in for the select area from (a) (b).

method dynamically adjusts the history weight α based on the current training loss, implementing an adaptive exponential moving average strategy. Specifically, the current loss value is linearly mapped to a predefined weight interval through:

$$\alpha = \alpha_{\text{max}} - \frac{L_{\text{clamp}} - L_{\text{min}}}{L_{\text{max}} - L_{\text{min}}} \cdot (\alpha_{\text{max}} - \alpha_{\text{min}}), \quad (14)$$

where $L_{\rm current}$ denotes the current loss value and $L_{\rm clamp} = \max(L_{\rm min}, \min(L_{\rm max}, L_{\rm current}))$ ensures the loss remains within the expected range $[L_{\rm min}, L_{\rm max}] = [10^{-6}, 10^{-2}]$, and the weight range is $[\alpha_{\rm min}, \alpha_{\rm max}] = [0.8, 0.99]$. Higher losses correspond to lower history weights, reducing the contribution of historical parameters. The parameter update follows:

TABLE II

AVERAGE PSNR/SSIM RESULTS ON CERES-50 DATASET FOR THE SENSITIVITY STUDY OF CONTRASTIVE WEIGHT θ_h in $4\times$ scale. Best Performance is shown in **BOLD**.

Method	0.1	0.2	0.3	0.4	0.5	0.6
HACBSR	29.83/0.719	29.83/0.720	29.86/0.720	29.87/0.720	29.85/0.720	29.84/0.719

TABLE III

AVERAGE PSNR/SSIM/LPIPS RESULTS ON CERES-50 DATASET FOR ABLATION ANALYSIS. THE NOTATION -CK DENOTES REMOVAL OF THE CONTRASTIVE KERNEL SAMPLING AND -CL DENOTES REMOVAL OF THE HISTORY-AUGMENT CONTRASTIVE LEARNING COMPONENT. BEST PERFORMANCE IS SHOWN IN **BOLD**.

Method	×2	×3	×4	Model Size
HACBSR	32.21/0.816/0.364	30.96/0.763/0.442	29.87/0.721/0.497	2359K + 562K
HACBSR (-CK)	31.99/0.815/0.372	30.91/0.762/0.443	29.81/0.720/0.500	2359K + 562K
HACBSR (-CL)	32.21 /0.814/0.365	30.92/0.762/0.448	29.75/0.720/0.526	2359K + 562K
HACBSR (-CK)(-CL)	31.99/0.815/0.370	30.89/0.762/ 0.444	29.77/0.720/0.499	2359K + 562K

$$\phi_{h,p+1}^x \leftarrow \alpha \phi_{h,p}^x + (1-\alpha)\phi_{i,p}^x,\tag{15}$$

where $\phi_{h,p}^x$ and $\phi_{i,p}^x$ represent historical and current parameters, respectively.

IV. EXPERIMENTS

A. Dataset and Data Preparation

To extend the application of planetary remote sensing, this work constructs the Ceres-50 dataset, a BSR dataset that includes 50 images. Ceres is a dwarf planet located in the asteroid belt that contains diverse geological and morphological features [44], [45], which are beneficial for future scientific analysis. The images of Ceres-50 are acquired from NASA's Small Bodies Node¹. The resolution of ground truth images is 1024 × 1024, and all images are grayscale. To simulate the degradation process in planetary remote sensing imaging, we construct a degradation model incorporating an anisotropic Gaussian kernel, bicubic downsampling, and additive Gaussian noise. The orbiter's compression system exhibits progressive degradation where compression ratios directly correlate with degradation severity [46].

B. Experiment details

This work employs U-Net as the network for image learning, consistent with DIP [11], [12], [14]. A two-layer MLP is used for kernel learning, with a hidden size of 1000. Experiments are conducted on an NVIDIA A100-SXM4-80GB GPU and an Intel Xeon Platinum 8168 CPU (16 cores), running Ubuntu 22.04.4 LTS, Python 3.12, and PyTorch 2.5.0 with CUDA 12.6. HACBSR is optimized for *N* 300 iterations. The learning rates for U-Net and the MLP are set to 0.005 and 0.5, respectively. During the Contrastive Image Learning stage, parameters are updated every 10 iterations. In each iteration, HACBSR processes a single image and performs unsupervised learning on the Ceres-50 images sequentially and each time conduct BSR on single image. For quantitative results, LPIPS

¹https://pdssbn.astro.umd.edu/

uses AlexNet as the encoder. The inner loop of P is set to 5 and the out loop of N is set to 300.

Quantitative results.

To evaluate the performance of the proposed method, comparative experiments were conducted against DDSR [14], MLMC [13], and FKP-DIP [11]. The comparative experimental results presented in Table I demonstrate that HACBSR achieves competitive performance across all tested scaling factors. To further validate the generalization capability of HACBSR, we performed additional experiments on the Ceres-50 dataset under noise-free conditions (without Additive Gaussian Noise), which shown in Table ??. It also shows that HACBSR achieves competitive performance on Ceres-50 dataset without Additive Gaussian Noise.

Qualitative results.

Figures 8, 9, and 10 present visual comparisons of different methods at $2\times$, $3\times$, and $4\times$ upscaling factors, respectively. The proposed HACBSR method demonstrates superior performance in both kernel reconstruction and image reconstruction across all scaling factors. This performance advantage is particularly evident at $4\times$ upscaling, where HACBSR maintains sharper edge preservation and produces more accurate kernel estimations compared to competing methods.

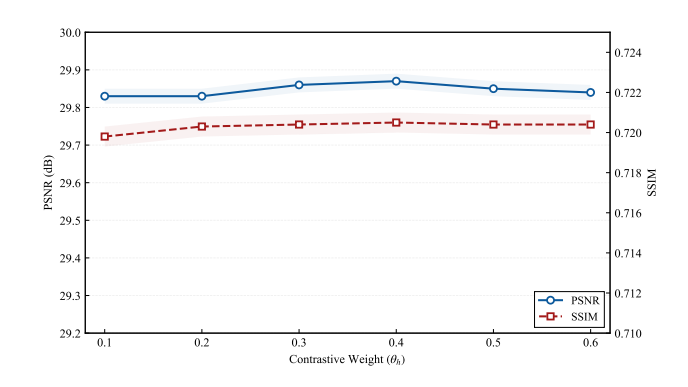


Fig. 11. Sensitivity study of contrastive weight θ_h on Ceres-50 dataset for $4\times$ scale.

C. Ablation Study

To validate the performance of key components in HACBSR, ablation experiments were conducted. The experimental results are presented in Table III. The results demonstrate that removing the Contrastive Kernel Generator significantly reduces PSNR and SSIM performance, particularly at lower BSR scales. Conversely, removing the Contrastive Learning (CL) component adversely affects reconstruction quality at higher BSR scales, with the most pronounced impact observed at $4\times$ scale. These experimental findings confirm that both the Contrastive Kernel Generator and Contrastive Learning components play critical roles in the overall performance of HACBSR.

D. Sensitivity Study of Hyperparameter

The contrastive weight θ_h controls the influence of history-augmented regularization in Equation 8. We investigate its effect on Ceres-50 at $4\times$ scale by varying θ_h across [0.1,0.6]. As shown in Figure 11 and Table II, HACBSR maintains consistent performance throughout this range. The optimal performance is achieved at $\theta_h=0.4$, with minimal performance variation observed at other values, demonstrating that HACBSR exhibits minimal sensitivity to θ_h variations. Unless otherwise stated, $\theta_h=0.4$ is used in all experiments.

V. CONCLUSION

This work introduces HACBSR, an unsupervised framework for blind super resolution in planetary remote sensing that not requires ground-truth images or kernel priors. HACBSR couples a kernel generator that learns random degradation kernels with a contrastive image estimator that utilizes contrastive negatives to enhance discrimination. On the Ceres-50 dataset with random Gaussian blur, additive Gaussian noise, and bicubic downsampling HACBSR achieves state-of-the-art performance among unsupervised methods, thereby validating both the kernel-learning stage and the contrastive image learning design. Importantly, our strong convexity analysis provides theoretical analysis for the convergence of history-augmented contrastive mechanism.

Despite these advances, the range of degradations explored remains constrained. Planetary remote sensing images often exhibit additional challenges such as striping noise, sensor artifacts, and missing-data masks, which are not fully addressed by the current framework. In future work, we will extend HACBSR to broader and more realistic degradation families, and develop mechanisms to handle occlusions and masks. We also plan to investigate stronger negative sampling strategies and adaptive kernel priors to further enhance reconstruction quality and robustness for planetary remote sensing.

REFERENCES

- C. Dong, C. C. Loy, K. He, and X. Tang, "Image super-resolution using deep convolutional networks," *IEEE transactions on pattern analysis* and machine intelligence, vol. 38, no. 2, pp. 295–307, 2015.
- [2] J. Kim, J. K. Lee, and K. M. Lee, "Accurate image super-resolution using very deep convolutional networks," in *Proceedings of the IEEE* conference on computer vision and pattern recognition, 2016, pp. 1646– 1654.

- [3] B. Lim, S. Son, H. Kim, S. Nah, and K. Mu Lee, "Enhanced deep residual networks for single image super-resolution," in *Proceedings* of the IEEE conference on computer vision and pattern recognition workshops, 2017, pp. 136–144.
- [4] M. Wei and X. Zhang, "Super-resolution neural operator," in *Proceedings of the IEEE/CVF Conference on Computer Vision and Pattern Recognition (CVPR)*, June 2023, pp. 18247–18256.
- [5] Y. Chen, S. Liu, and X. Wang, "Learning continuous image representation with local implicit image function," in *Proceedings of the IEEE/CVF* conference on computer vision and pattern recognition, 2021, pp. 8628– 8638.
- [6] H.-J. Zhao, J. Lu, W.-X. Guo, and X.-P. Lu, "Neural operator for planetary remote sensing super-resolution with spectral learning," *Mathematics*, vol. 12, no. 22, p. 3461, 2024.
- [7] S. Bell-Kligler, A. Shocher, and M. Irani, "Blind super-resolution kernel estimation using an internal-gan," Advances in neural information processing systems, vol. 32, 2019.
- [8] K. Zhang, W. Zuo, Y. Chen, D. Meng, and L. Zhang, "Beyond a gaussian denoiser: Residual learning of deep cnn for image denoising," *IEEE transactions on image processing*, vol. 26, no. 7, pp. 3142–3155, 2017.
- [9] X. Kang, J. Li, P. Duan, F. Ma, and S. Li, "Multilayer degradation representation-guided blind super-resolution for remote sensing images," *IEEE Transactions on Geoscience and Remote Sensing*, vol. 60, pp. 1– 12, 2022
- [10] Z. Liang, S. Wang, T. Zhang, and Y. Fu, "Blind super-resolution of single remotely sensed hyperspectral image," *IEEE Transactions on Geoscience* and Remote Sensing, vol. 61, pp. 1–14, 2023.
- [11] J. Liang, K. Zhang, S. Gu, L. Van Gool, and R. Timofte, "Flow-based kernel prior with application to blind super-resolution," arXiv preprint arXiv:2103.15977, 2021.
- [12] D. Ulyanov, A. Vedaldi, and V. Lempitsky, "Deep image prior," in Proceedings of the IEEE conference on computer vision and pattern recognition, 2018, pp. 9446–9454.
- [13] J. Xia, Z. Yang, S. Li, S. Zhang, Y. Fu, D. Gündüz, and X. Li, "Blind super-resolution via meta-learning and markov chain monte carlo simulation," *IEEE Transactions on Pattern Analysis and Machine Intelligence*, 2024.
- [14] Z. Yang, J. Xia, S. Li, W. Liu, S. Zhi, S. Zhang, L. Liu, Y. Fu, and D. Gündüz, "Meta-learning based blind image super-resolution approach to different degradations," *Neural Networks*, vol. 178, p. 106429, 2024.
- [15] A. Liu, Y. Liu, J. Gu, Y. Qiao, and C. Dong, "Blind image superresolution: A survey and beyond," *IEEE transactions on pattern analysis* and machine intelligence, vol. 45, no. 5, pp. 5461–5480, 2022.
- [16] Y. Zhang, K. Li, K. Li, L. Wang, B. Zhong, and Y. Fu, "Image superresolution using very deep residual channel attention networks," in *Proceedings of the European conference on computer vision (ECCV)*, 2018, pp. 286–301.
- [17] K. Zhang, L. V. Gool, and R. Timofte, "Deep unfolding network for image super-resolution," in *Proceedings of the IEEE/CVF conference* on computer vision and pattern recognition, 2020, pp. 3217–3226.
- [18] K. Zhang, W. Zuo, and L. Zhang, "Learning a single convolutional superresolution network for multiple degradations," in *Proceedings of the IEEE conference on computer vision and pattern recognition*, 2018, pp. 3262–3271.
- [19] K. Chauhan, S. N. Patel, M. Kumhar, J. Bhatia, S. Tanwar, I. E. Davidson, T. F. Mazibuko, and R. Sharma, "Deep learning-based single-image super-resolution: A comprehensive review," *IEEE Access*, vol. 11, pp. 21811–21830, 2023.
- [20] J. Gu, H. Lu, W. Zuo, and C. Dong, "Blind super-resolution with iterative kernel correction," in *Proceedings of the IEEE/CVF conference* on computer vision and pattern recognition, 2019, pp. 1604–1613.
- [21] H. Su, Y. Li, Y. Xu, X. Fu, and S. Liu, "A review of deep-learning-based super-resolution: From methods to applications," *Pattern Recognition*, vol. 157, p. 110935, 2025.
- [22] Y. Wang, L. Wang, H. Wang, and P. Li, "Resolution-aware network for image super-resolution," *IEEE Transactions on Circuits and Systems for Video Technology*, vol. 29, no. 5, pp. 1259–1269, 2018.
- [23] J. Lei, Z. Zhang, X. Fan, B. Yang, X. Li, Y. Chen, and Q. Huang, "Deep stereoscopic image super-resolution via interaction module," *IEEE Transactions on Circuits and Systems for Video Technology*, vol. 31, no. 8, pp. 3051–3061, 2020.
- [24] Y. Zhang, Y. Tian, Y. Kong, B. Zhong, and Y. Fu, "Residual dense network for image super-resolution," in *Proceedings of the IEEE conference on computer vision and pattern recognition*, 2018, pp. 2472–2481.
- [25] J. Li, F. Fang, K. Mei, and G. Zhang, "Multi-scale residual network for image super-resolution," in *Proceedings of the European conference on* computer vision (ECCV), 2018, pp. 517–532.

- [26] Y. Mo, Y. Wang, C. Xiao, J. Yang, and W. An, "Dense dual-attention network for light field image super-resolution," *IEEE Transactions on Circuits and Systems for Video Technology*, vol. 32, no. 7, pp. 4431–4443, 2021.
- [27] Z. Wang, L. Li, Y. Xue, C. Jiang, J. Wang, K. Sun, and H. Ma, "Fenet: Feature enhancement network for lightweight remote-sensing image super-resolution," *IEEE Transactions on Geoscience and Remote Sensing*, vol. 60, pp. 1–12, 2022.
- [28] J. Wang, B. Wang, X. Wang, Y. Zhao, and T. Long, "Hybrid attention based u-shaped network for remote sensing image super-resolution," *IEEE Transactions on Geoscience and Remote Sensing*, 2023.
- [29] A. Shocher, N. Cohen, and M. Irani, ""zero-shot" super-resolution using deep internal learning," in *Proceedings of the IEEE conference on computer vision and pattern recognition*, 2018, pp. 3118–3126.
- [30] J. W. Soh, S. Cho, and N. I. Cho, "Meta-transfer learning for zeroshot super-resolution," in *Proceedings of the IEEE/CVF conference on* computer vision and pattern recognition, 2020, pp. 3516–3525.
- [31] Y. Qiu, Q. Zhu, S. Zhu, and B. Zeng, "Dual circle contrastive learning-based blind image super-resolution," *IEEE Transactions on Circuits and Systems for Video Technology*, vol. 34, no. 3, pp. 1757–1771, 2023.
- [32] Z. Luo, H. Huang, L. Yu, Y. Li, B. Zeng, and S. Liu, "Kernel reformulation with deep constrained least squares for blind image super-resolution," *IEEE Transactions on Circuits and Systems for Video Technology*, 2025.
- [33] K. Zhang, Y. Li, W. Zuo, L. Zhang, L. Van Gool, and R. Timofte, "Plugand-play image restoration with deep denoiser prior," *IEEE Transactions* on Pattern Analysis and Machine Intelligence, vol. 44, no. 10, pp. 6360– 6376, 2021.
- [34] J. Zhang, S. Lu, F. Zhan, and Y. Yu, "Blind image super-resolution via contrastive representation learning," arXiv preprint arXiv:2107.00708, 2021
- [35] Z. Liang, S. Wang, T. Zhang, and Y. Fu, "Blind super-resolution of single remotely sensed hyperspectral image," *IEEE Transactions on Geoscience* and Remote Sensing, 2023.
- [36] N. Zhang, Y. Wang, X. Zhang, D. Xu, X. Wang, G. Ben, Z. Zhao, and Z. Li, "A multi-degradation aided method for unsupervised remote sensing image super resolution with convolution neural networks," *IEEE Transactions on Geoscience and Remote Sensing*, vol. 60, pp. 1–14, 2020
- [37] Y. Xiao, Q. Yuan, Q. Zhang, and L. Zhang, "Deep blind super-resolution for satellite video," *IEEE Transactions on Geoscience and Remote Sensing*, vol. 61, pp. 1–16, 2023.
- [38] H. Hu, X. Wang, Y. Zhang, Q. Chen, and Q. Guan, "A comprehensive survey on contrastive learning," *Neurocomputing*, p. 128645, 2024.
- [39] A. Jaiswal, A. R. Babu, M. Z. Zadeh, D. Banerjee, and F. Makedon, "A survey on contrastive self-supervised learning," *Technologies*, vol. 9, no. 1, p. 2, 2020.
- [40] Z. Wu, Y. Xiong, S. X. Yu, and D. Lin, "Unsupervised feature learning via non-parametric instance discrimination," in *Proceedings of the IEEE* conference on computer vision and pattern recognition, 2018, pp. 3733– 3742.
- [41] K. He, H. Fan, Y. Wu, S. Xie, and R. Girshick, "Momentum contrast for unsupervised visual representation learning," in *Proceedings of the IEEE/CVF conference on computer vision and pattern recognition*, 2020, pp. 9729–9738.
- [42] G. Wu, J. Jiang, K. Jiang, and X. Liu, "Learning from history: Task-agnostic model contrastive learning for image restoration," in *Proceedings of the AAAI Conference on Artificial Intelligence*, vol. 38, no. 6, 2024, pp. 5976–5984.
- [43] A. Radford, J. W. Kim, C. Hallacy, A. Ramesh, G. Goh, S. Agarwal, G. Sastry, A. Askell, P. Mishkin, J. Clark et al., "Learning transferable visual models from natural language supervision," in *International* conference on machine learning. PmLR, 2021, pp. 8748–8763.
- conference on machine learning. PmLR, 2021, pp. 8748–8763.
 [44] T. B. McCord, J.-P. Combe, J. C. Castillo-Rogez, H. Y. McSween, and T. H. Prettyman, "Ceres, a wet planet: The view after dawn," Geochemistry, vol. 82, no. 2, p. 125745, 2022.
- [45] C. Russell, C. Raymond, E. Ammannito, D. Buczkowski, M. C. De Sanctis, H. Hiesinger, R. Jaumann, A. Konopliv, H. McSween, A. Nathues *et al.*, "Dawn arrives at ceres: Exploration of a small, volatile-rich world," *Science*, vol. 353, no. 6303, pp. 1008–1010, 2016.
- [46] H. Sierks, H. Keller, R. Jaumann, H. Michalik, T. Behnke, F. Bubenhagen, I. Büttner, U. Carsenty, U. Christensen, R. Enge et al., "The dawn framing camera," Space science reviews, vol. 163, pp. 263–327, 2011.

APPENDIX

STABILITY ANALYSIS OF HISTORY-AUGMENTED CONTRASTIVE LEARNING

This section provides a mathematics analysis of the stability property introduced for the history-augmented contrastive learning mechanism in the HACBSR framework, recast through the lens of strong convexity. In particular, we show that the historical contrastive term induces a strong convexity that governs the stability constant and renders the update non-expansive in the feature metric.

PROBLEM FORMULATION AND KEY ASSUMPTIONS

Following section III, we consider the BSR problem under the degradation model:

$$\mathbf{y} = (\mathbf{x} \otimes \mathbf{k}) \downarrow_s + \mathbf{z},\tag{16}$$

where $\mathbf{y} \in \mathbb{R}^{H \times W}$ is the observed LR image, $\mathbf{x} \in \mathbb{R}^{sH \times sW}$ is the HR image, \otimes denotes 2D convolution, \downarrow_s denotes downsampling by factor s, \mathbf{k} is an unknown blur kernel, and \mathbf{z} represents random noise.

In the Contrastive Image Learning (CIL) stage, the model optimizes an image estimator G_x and a kernel generator G_k using the Formula 8. For concise proof, we consider the following objective:

$$L(\mathbf{x}, \mathbf{x}_h) = \underbrace{\|\mathbf{y} - \mathcal{A}_k \mathbf{x}\|_F^2}_{\text{Observation Consistency}} + \theta_h \underbrace{\|f_c(\mathbf{x}) - f_c(\mathbf{x}_h)\|_F^2}_{\text{History-augmented Contrastive Learning}}$$
(17)

where $\mathcal{A}_k \mathbf{x} = (\mathbf{x} \otimes \mathbf{k}) \downarrow_s$ is the linear degradation operator, $\mathbf{x}_h = G_x(z_x, \phi_{x,h}^{\mathrm{CIL}})$ is the historical SR estimate, f_c is a feature encoder, and $\theta_h > 0$ controls the strength of historical regularization.

To facilitate analysis, we make the following key assumption to simplify the further analysis:

• Linearity of f_c : The feature encoder f_c is a linear transformation with matrix representation \mathbf{B} , such that $f_c(\mathbf{x}) = \mathbf{B}\mathbf{x}$ under vectorization.

Let A_k denote the matrix representation of A_k . Define the system matrix and its strong convexity constant:

$$\mathbf{M}(\theta_h) = \mathbf{A}_k^{\top} \mathbf{A}_k + \theta_h \mathbf{B}^{\top} \mathbf{B}, \qquad \mu(\theta_h) \triangleq \lambda_{\min} (\mathbf{M}(\theta_h)).$$
(18)

We assume $\mathbf{M}(\theta_h)$ is positive definite, so the solution is unique. The quantity $\mu(\theta_h)$ will be referred to as the *strong convexity constant*, which increases with θ_h .

STABILITY ANALYSIS VIA STRONG CONVEXITY

Under the assumptions in Section A, let \mathbf{x}^* be the solution of $L(\mathbf{x}, \mathbf{x}_h)$ in (17). Then the deviation in the feature space between \mathbf{x}^* and the historical estimate \mathbf{x}_h admits the following consistency bound:

$$||f_c(\mathbf{x}^*) - f_c(\mathbf{x}_h)||_F \le C(k, \theta_h) ||\mathbf{y} - \mathcal{A}_k \mathbf{x}_h||_F,$$
 (19)

where the stability constant $C(k, \theta_h)$ is defined as

$$C(k, \theta_h) = \|\mathbf{B} \mathbf{M}(\theta_h)^{-1} \mathbf{A}_k^{\top}\|_2. \tag{20}$$

Moreover, the following properties hold:

 Control by the strong convexity. The stability constant is bounded by

$$C(k, \theta_h) \le \frac{\|\mathbf{B}\|_2 \|\mathbf{A}_k\|_2}{\mu(\theta_h)} = \frac{\|\mathbf{B}\|_2 \|\mathbf{A}_k\|_2}{\lambda_{\min}(\mathbf{M}(\theta_h))},$$
 (21)

and is nonincreasing with respect to θ_h .

2) Asymptotic decay under informative features. If the feature encoder B has a positive minimum singular value $(\sigma_{\min}(\mathbf{B}) > 0)$, then

$$||f_c(\mathbf{x}^*) - f_c(\mathbf{x}_h)||_F \le \frac{||\mathbf{B}||_2 ||\mathbf{A}_k||_2}{\theta_h \lambda_{\min}(\mathbf{B}^\top \mathbf{B})} ||\mathbf{y} - \mathcal{A}_k \mathbf{x}_h||_F,$$
(22)

which tends to 0 as $\theta_h \to \infty$.

a) *Proof.*: We work with vectorized images and linear operators. The objective in (17) becomes

$$L(\mathbf{x}, \mathbf{x}_h) = \|\mathbf{y} - \mathbf{A}_k \mathbf{x}\|_2^2 + \theta_h \|\mathbf{B}(\mathbf{x} - \mathbf{x}_h)\|_2^2.$$

Since $\mathbf{M}(\theta_h)$ is positive definite, Φ_k is strictly convex and has the unique solution \mathbf{x}^* satisfying the normal equations:

$$(\mathbf{A}_k^{\mathsf{T}} \mathbf{A}_k + \theta_h \mathbf{B}^{\mathsf{T}} \mathbf{B}) \mathbf{x}^{\star} = \mathbf{A}_k^{\mathsf{T}} \mathbf{y} + \theta_h \mathbf{B}^{\mathsf{T}} \mathbf{B} \mathbf{x}_h. \tag{23}$$

Subtracting $\mathbf{M}(\theta_h)\mathbf{x}_h$ from both sides yields the perturbation form

$$\mathbf{M}(\theta_h) (\mathbf{x}^* - \mathbf{x}_h) = \mathbf{A}_k^{\top} (\mathbf{y} - \mathbf{A}_k \mathbf{x}_h), \tag{24}$$

and hence

$$\mathbf{x}^{\star} - \mathbf{x}_h = \mathbf{M}(\theta_h)^{-1} \mathbf{A}_k^{\top} (\mathbf{y} - \mathbf{A}_k \mathbf{x}_h). \tag{25}$$

Applying B, taking norms, and using submultiplicativity gives

$$\|\mathbf{B}(\mathbf{x}^{\star} - \mathbf{x}_h)\|_2 \leq \|\mathbf{B} \mathbf{M}(\theta_h)^{-1} \mathbf{A}_k^{\top}\|_2 \cdot \|\mathbf{y} - \mathbf{A}_k \mathbf{x}_h\|_2$$

which proves (19) with $C(k, \theta_h)$ as in (20). To obtain (21), apply submultiplicativity again:

$$C(k, \theta_h) \leq \|\mathbf{B}\|_2 \cdot \|\mathbf{M}(\theta_h)^{-1}\|_2 \cdot \|\mathbf{A}_k^{\top}\|_2 = \frac{\|\mathbf{B}\|_2 \|\mathbf{A}_k\|_2}{\lambda_{\min}(\mathbf{M}(\theta_h))}$$
$$= \frac{\|\mathbf{B}\|_2 \|\mathbf{A}_k\|_2}{\mu(\theta_h)}.$$
 (26)

The monotonicity of $C(k,\theta_h)$ follows from the Loewner order: for $\theta_h' > \theta_h$, we have $\mathbf{M}(\theta_h') \succeq \mathbf{M}(\theta_h)$, hence $\mathbf{M}(\theta_h')^{-1} \preceq \mathbf{M}(\theta_h)^{-1}$ and $\|\mathbf{M}(\theta_h')^{-1}\|_2 \leq \|\mathbf{M}(\theta_h)^{-1}\|_2$.

Finally, to prove the asymptotic result (22), we lower-bound the minimum eigenvalue via Weyl's inequality:

$$\lambda_{\min}(\mathbf{M}(\theta_h)) = \lambda_{\min}(\mathbf{A}_k^{\top} \mathbf{A}_k + \theta_h \mathbf{B}^{\top} \mathbf{B})$$

$$\geq \lambda_{\min}(\mathbf{A}_k^{\top} \mathbf{A}_k) + \theta_h \lambda_{\min}(\mathbf{B}^{\top} \mathbf{B}) \qquad (27)$$

$$\geq \theta_h \lambda_{\min}(\mathbf{B}^{\top} \mathbf{B}).$$

Substituting this into (21) yields

$$||f_c(\mathbf{x}^*) - f_c(\mathbf{x}_h)||_F \le \frac{||\mathbf{B}||_2 ||\mathbf{A}_k||_2}{\theta_h \lambda_{\min}(\mathbf{B}^\top \mathbf{B})} \cdot ||\mathbf{y} - \mathcal{A}_k \mathbf{x}_h||_F,$$

which clearly tends to 0 as $\theta_h \to \infty$.

b) Conclusion.: The historical contrastive term $\theta_h \| \mathbf{B}(\mathbf{x} - \mathbf{x}_h) \|_2^2$ increases the strong convexity constant $\mu(\theta_h) = \lambda_{\min}(\mathbf{M}(\theta_h))$, thereby shrinking the stability constant $C(k,\theta_h)$ in (19). Consequently, the gradient update becomes more stable and renders the update non-expansive in the feature metric. As θ_h grows, the constant increases and the feature-space deviation is uniformly bounded and vanishes asymptotically, stabilizing optimization while balancing observation consistency and historical coherence.